
UNDERSTANDING FRANK-WOLFE ADVERSARIAL TRAINING

PREPRINT

Theodoros Tsiligkaridis*, **Jay Roberts***
 Massachusetts Institute of Technology Lincoln Laboratory
 Lexington, MA 02421
 {ttsili, jay.roberts}@ll.mit.edu

June 15, 2022

ABSTRACT

Deep neural networks are easily fooled by small perturbations known as adversarial attacks. Adversarial Training (AT) is a technique that approximately solves a robust optimization problem to minimize the worst-case loss and is widely regarded as the most effective defense against such attacks. While projected gradient descent (PGD) has received most attention for approximately solving the inner maximization of AT, Frank-Wolfe (FW) optimization is projection-free and can be adapted to any ℓ_p norm. A Frank-Wolfe adversarial training approach is presented and is shown to provide as competitive level of robustness as PGD-AT for a variety of architectures, attacks, and datasets. Exploiting a representation of the FW attack we are able to derive the geometric insight that: The larger the ℓ_2 norm of an ℓ_∞ attack is, the less loss gradient variation there is. It is then experimentally demonstrated that ℓ_∞ attacks against robust models achieve near the maximal possible ℓ_2 distortion, providing a new lens into the specific type of regularization that AT bestows. Using FW optimization in conjunction with robust models, we are able to generate sparse human-interpretable counterfactual explanations without relying on expensive ℓ_1 projections.

1 Introduction

Deep neural networks (DNN) are powerful models that have achieved excellent performance across various domains LeCun et al. [2015]. As these models are being deployed across industries, such as healthcare and autonomous driving, robustness and interpretability concerns become increasingly important. Several organizations have also have identified important principles of artificial intelligence (AI) that include notions of reliability and transparency Pichai [2018], Microsoft [2019], Lopez [2020].

One issues of such large capacity models is that small, carefully chosen input perturbations, known as adversarial perturbations, can lead to incorrect predictions Goodfellow et al. [2015]. Various enhancement methods have been proposed to defend against adversarial perturbations Kurakin et al. [2017], Ros and Doshi-Velez [2018], Madry et al. [2018], Moosavi-Dezfooli et al. [2019]. One of the best performing algorithms is adversarial training (AT) Madry et al. [2018], which is formulated as a robust optimization problem Shaham et al. [2018]. Computation of optimal adversarial perturbations is NP-hard Weng et al. [2018] and approximate methods are used to solve the inner maximization. The most popular approximate method that has been proven to be successful is projected gradient descent (PGD). Training against weaker attacks can reduce the computational cost but leads to strong robustness against weak attacks and brittleness against stronger attacks. This can be due to gradient obfuscation Uesato et al. [2018], Athalye et al. [2018], a phenomena where networks learn to defend against gradient-based attacks by making the loss landscape highly non-linear. Another sign of gradient obfuscation is when adversarial attacks computed with a few iterations fail but black-box attacks successfully find adversarial perturbations Uesato et al. [2018], Guo et al. [2019]. Frank-Wolfe (FW) optimization has been recently proposed in Chen et al. [2020] and was shown to effectively fool standard networks with less distortion.

* Authors have made equal contributions.

Another major concern is interpretability of DNN decisions and explanation methods for AI system users or stakeholders. Some popular explanation methods include layerwise relevance propagation (LRP) Bach et al. [2015], locally interpretable model-agnostic explanations Ribeiro et al. [2016], and contrastive explanations Dhurandhar et al. [2019], but these methods only yield feature relevance and are susceptible to spurious correlations prevalent in standard networks Ilyas et al. [2019]. The relationship between adversarial robustness and saliency map interpretability was recently studied in Etmann et al. [2019] but experiments were based on gradient regularization.

Insights into model behavior based on counterfactual explanations based on adversarial perturbations have the potential to be very useful for users Wachter et al. [2018]. However, standard networks do not have interpretable saliency maps and adversarial attacks tend to be visually imperceptible. Furthermore, recent works Tsipras et al. [2019], Ilyas et al. [2019] claim that existence of adversarial examples are due to standard training methods that rely on highly predictive but non-robust features, and make connections between robustness and explainability. These results highlight the importance of using robust models when explainability is desired.

In this paper, we propose a Frank-Wolfe adversarial training (FW-AT) method as a way to obtain robustness on par with PGD-AT while providing a level of mathematical transparency which PGD lacks. This allows us to derive relationships between adversarial perturbations' distortion and the structure of the loss landscape. Our main contributions are summarized below:

- An adversarial training method based on Frank-Wolfe (FW-AT) is presented that is projection-free and is trivially adaptable to arbitrary ℓ_p norm.
- Theoretical guarantees are derived to relate the local geometry of the loss to the magnitude of the FW adversarial perturbation in the ℓ_∞ norm case. The theory shows that higher distortion ℓ_∞ perturbations imply less directional variation of loss gradients and we demonstrate empirically that robust models achieve the near maximal distortion.
- It is shown that FW-AT achieves high adversarial robustness similar to PGD-AT for a variety of architectures when evaluated against strong white-box and black-box attacks demonstrating strong resistance to gradient masking.
- Using a modified FW optimization, we efficiently generate sparse counterfactual explanations to explain model predictions.

2 Background and Previous Work

Consider $(x_i, y_i) \sim \mathcal{D}$ pairs of data examples drawn from distribution \mathcal{D} . The labels span C classes. The neural network function $f_\theta(\cdot)$ maps input features into logits, where θ are the model parameters. The class probability scores are obtained using the softmax transformation $p_c(x) = e^{f_{\theta,c}(x)} / \sum_l e^{f_{\theta,l}(x)}$. The predicted class label is given by $\hat{y}(x) = \arg \max_c f_{\theta,c}(x)$.

2.1 Adversarial Robustness

The prevalent way of training classifiers is through empirical risk minimization (ERM):

$$\min_{\theta} \mathbb{E}_{(x,y) \sim \mathcal{D}} [\mathcal{L}(x, y; \theta)] \quad (1)$$

where the loss is the cross-entropy loss function given by $\mathcal{L}(f_\theta(x), y) = \mathcal{L}(x, y; \theta) = -y^T \log(p_\theta(x))$ and y denotes the one-hot label vector.

Adversarial robustness for a classifier f_θ is defined with respect to a metric, here chosen as the ℓ_p metric associated with the ball $B_p(\epsilon) = \{\delta : \|\delta\|_p \leq \epsilon\}$, as follows. A network is said to be robust to adversarial perturbations of size ϵ at a given input example x iff $\hat{y}(x) = \hat{y}(x + \delta)$ for all $\delta \in B_p(\epsilon)$, i.e., if the predicted label does not change for all perturbations of size up to ϵ . The ϵ is often referred to as the strength or budget of the attack.

Training neural networks using the ERM principle (1) gives high accuracy on test sets but leaves the network vulnerable to adversarial attacks. One of the most effective defenses against such attacks is adversarial training (AT) Madry et al. [2018] which minimizes the adversarial risk instead,

$$\min_{\theta} \mathbb{E}_{(x,y) \sim \mathcal{D}} \left[\max_{\delta \in B_p(\epsilon)} \mathcal{L}(x + \delta, y; \theta) \right]. \quad (2)$$

The training procedure constructs adversarial attacks at given inputs x that solve the inner maximization problem. Common maximization methods typically use a fixed number of gradient-ascent steps. One such method is projected

gradient descent (PGD) that performs the iterative updates:

$$\delta^{(k+1)} = P_{B_p(\epsilon)} \left(\delta^{(k)} + \alpha \nabla_{\delta} \mathcal{L}(x + \delta^k, y; \theta) \right) \quad (3)$$

where $P_{B_p(\epsilon)}(z) = \arg \min_{u \in B_p(\epsilon)} \|z - u\|_2^2$ denotes the orthogonal projection onto the constraint set. The sign of the gradient has also been shown to be an effective perturbation. The computational cost of this method is dominated by the number of steps used to approximate the inner maximization, since a K step PGD approximation to the maximization involves K forward-backward propagations through the network. While using fewer PGD steps can lower this cost, these amount to weaker attacks which can lead to gradient obfuscation Papernot et al. [2017], Uesato et al. [2018]. Another method akin to adversarial training is TRADES Zhang et al. [2019] which proposes a modified loss function that captures the clean and adversarial accuracy tradeoff and still relies on PGD adversarial attack generation.

Prior works on regularization for adversarial robustness include gradient Lyu et al. [2015], Ros and Doshi-Velez [2018] and curvature Moosavi-Dezfooli et al. [2019] regularization. Gradient regularization has not been shown to yield good robustness against strong attacks, while the relationship between small curvature and high robustness has been better established, but still leaves significant room for improvement. Based on the connection between curvature and robustness, a regularizer that promotes local linearity near training examples was proposed in Qin et al. [2019] that is based on an iterative method leading to similar computational cost as PGD-AT. These methods argue that flattening the decision boundary via the loss is a suitable defense against adversarial attacks. Many defenses have been shown to be evaded by newer attacks while adversarial training has been demonstrated to maintain state-of-the-art robustness Athalye et al. [2018]. We develop a Frank-Wolfe adversarial training approach that is competitive with PGD-AT while offering increased transparency through an analytical expression for adversarial perturbations and distortion analysis that relates to the local loss geometry.

2.2 Counterfactual Explanations

Explanation methods based on counterfactual reasoning have been proposed in Wachter et al. [2018] and seek to provide the minimal, or otherwise sparse, amount of change in order to change a prediction. In particular, given an input x and distance metric d , a counterfactual explanation c is obtained by solving

$$\min_c d(x, c) \text{ s.t. } \hat{y}(x) \neq \hat{y}(c) \quad (4)$$

where \hat{y} denotes the prediction. Several works have studied finding nearest-neighbors of an input example that has a different prediction Mothilal et al. [2020], Karimi et al. [2020]. Changing the prediction of a standard model in image space leads to imperceptible adversarial perturbations. For this reason, several works for visual counterfactual generation based on generative models Samangouei et al. [2018], Chang et al. [2019] or group-sparse attacks (used as explanations) have been proposed to identify minimal sufficient regions instead of imperceptible changes Xu et al. [2019]. Robust models have been shown to change decisions when class-specific feature emerge in the image Tsipras et al. [2019], which makes them strong candidates for providing human-interpretable counterfactuals. We demonstrate that our Frank-Wolfe framework, in conjunction with robust models, is able to generate minimal or sparse counterfactual perturbations with significant semantic structure.

3 Frank-Wolfe Adversarial Training

PGD-AT trains models on the worst case loss and requires careful tuning of the step size Wong et al. [2020]. Choosing the step size α too small results in attacks which require many steps and choosing it too large results in iterations that leave the constraint set several times and may overshoot leading to suboptimal adversarial examples Wang et al. [2019]. In our experiments we choose the step size to be $b\epsilon/K$ with $b \geq 1.5$ for K -step PGD to allow sufficient exploration of the boundary.

These observations lead us to consider a Frank-Wolfe (FW) optimization algorithm Frank and Wolfe [1956], Jaggi [2013]. This method optimizes a linear approximation to the optimization, called a Linear Maximization Oracle (LMO), at each iteration,

$$LMO = \bar{\delta}^k = \operatorname{argmax}_{\delta \in B_p(\epsilon)} \langle \delta, \nabla_{\delta} \mathcal{L}(x + \delta^k, y) \rangle.$$

After calling LMO, FW stakes a step using a convex combination with the current iterate,

$$\delta^{k+1} = \delta^k + \gamma^k (\bar{\delta}^k - \delta^k)$$

where $\gamma^k \in [0, 1]$ is the step size. Optimizing step sizes can be found at additional computational cost; however, in practice an effective choice is $\gamma^k = c/(c + k)$ for some $c \geq 1$. Experiments show robustness of FW-AT is not sensitive to choice of c .

For general non-convex constrained optimization the Frank-Wolfe gap Frank and Wolfe [1956]:

$$g(\delta^k) = \max_{\delta \in B_p(\epsilon)} \langle \delta - \delta^k, \nabla_{\delta} \mathcal{L}(x + \delta^k, y) \rangle \quad (5)$$

is the convergence criterion considered. In general $g(\delta^k) \geq 0$ and δ^k is a stationary point if and only if $g(\delta^k) = 0$. Since the FW method calls the LMO oracle, a loss improvement proportional to the FW gap is expected, i.e. $\mathcal{L}(x^{k+1}, y) \approx \mathcal{L}(x^k, y) + \gamma^k g(\delta^k)$.

3.1 Closed-form solution to LMO

The FW sub-problem can be solved exactly for any ℓ_p and the optimal $\bar{\delta}^k$ is given by $\bar{\delta}_i^k = \epsilon \phi_p(\nabla \mathcal{L}_i^k)$, where

$$\phi_p(\nabla \mathcal{L}_i^k) = \text{sgn}(\nabla \mathcal{L}_i^k) \begin{cases} e_i^{i_k^*}, & p = 1 \\ \frac{|\nabla \mathcal{L}_i^k|^{q/p}}{\|\nabla \mathcal{L}_i^k\|_q^{q/p}}, & 1 < p < \infty \\ 1, & p = \infty \end{cases} \quad (6)$$

$\nabla \mathcal{L} = \nabla_{\delta} \mathcal{L}(x + \delta^k, y)$, and $1/p + 1/q = 1$. For $p = 1$, $i_k^* = \text{argmax}_i |\nabla \mathcal{L}_i^k|$ and $e^{i_k^*}$ is equal to 1 for the i_k^* -th component and zero otherwise.

FW does not require a projection onto the ℓ_p ball which is non-trivial for p not in $\{2, \infty\}$. Interestingly, for the special case of ℓ_{∞} attacks the optimal solution becomes the signed gradient of the loss, i.e. $\bar{\delta}^k = \epsilon \text{sgn}(\nabla_{\delta} \mathcal{L}(x + \delta^k))$ which matches the Fast Gradient Sign Method (FGSM) of adversarial attacks Goodfellow et al. [2015].

3.2 Distortion Analysis for Robustness

Though all ℓ_p attacks must remain in $B_p(\epsilon)$ their ℓ_q norms, for $q \neq p$, can be quite different. This is referred to as distortion and in particular for ℓ_{∞} attacks we are interested in what insight the ℓ_2 distortion can give us into the behavior of the attack.

It has been empirically observed in recent work Chen et al. [2020] that FW achieves a lower distortion than PGD attacks for standard networks while still achieving high success rates. Figure 1 illustrates this empirically on three architectures trained with ERM (1) and PGD(10)-AT (2)² on CIFAR-10. We analyze the max distortion ratio of ℓ_{∞} FW(20) and PGD(20) attacks of strength $\epsilon = 8/255$ on the CIFAR10 test dataset. Note that the maximum distortion possible is $\epsilon\sqrt{d}$.

The first row of Figure 1 shows that adversarial perturbations of robust models produce attacks that are nearly maximally distorted for both PGD and FW. In the case of FW attacks we have developed a rigorous theory as to why this is the case.

Our primary tool in analyzing the distortion of FW attacks, and a prime reason FW-AT is more mathematically transparent than PGD-AT, is that we may express a FW attack as a convex combination of the LMO iterates.

Proposition 1. *The FW-AT Algorithm with step sizes $\gamma^k = c/(c + k)$ for some $c \geq 1$ yields the following adversarial perturbation after K steps*

$$\delta^K = \epsilon \sum_{l=0}^{K-1} \alpha^l \phi_p(\nabla_{\delta} \mathcal{L}(x + \delta^l, y)) \quad (7)$$

where $\alpha^l = \gamma^l \prod_{i=l+1}^{K-1} (1 - \gamma^i) \in [0, 1]$ are non-decreasing in l , and sum to unity.

Proposition 1 shows that the FW adversarial perturbation may be expressed as a convex combination of the scaled loss gradients. Furthermore, for $c = 1$ all coefficients are uniform $\alpha^l = 1/K$ while larger $c > 1$ leads to a slower step-size decay and places more weight on later steps.

Theorem 1. *Consider the FW-AT Algorithm 1 and the ℓ_{∞} norm case. Let $\cos \beta^{lj}$ be the directional cosine between $\text{sgn}(\nabla_{\delta} \mathcal{L}(x + \delta^l, y))$ and $\text{sgn}(\nabla_{\delta} \mathcal{L}(x + \delta^j, y))$. The maximal ℓ^2 distortion ratio of the adversarial perturbation δ^K is:*

$$\frac{\|\delta^K\|_2}{\epsilon\sqrt{d}} = \sqrt{1 - 2 \sum_{l < j} \alpha^l \alpha^j (1 - \cos \beta^{lj})} \quad (8)$$

The spirit of Theorem 1 can be summarized as: Higher distortion of ℓ_{∞} attack implies lower loss gradient variation. The following theorem makes this precise.

²The same behavior occurs for FW(10)-AT robust model

Theorem 2. *Let the same conditions as Theorem 1 hold and $K > 1$. Assume the maximal ℓ_2 distortion ratio of the adversarial perturbation satisfies:*

$$\frac{\|\delta^K\|_2}{\epsilon\sqrt{d}} \geq \sqrt{1-\eta}$$

for some $\eta \in (0, 1)$. Then, the following hold.

1. *Bounded number of sign changes:*

$$\sum_{l < j} \frac{n^{lj}}{d} \leq \frac{\eta}{4\alpha^0\alpha^1} \quad (9)$$

where n^{lj} is the number of sign changes between the gradients at $x + \delta^l$ and $x + \delta^j$

2. *Bounded deviation away from FGSM step:*

$$\frac{\|\delta^K - \epsilon \text{sgn}(\nabla_x \mathcal{L}(x, y))\|_2}{\epsilon\sqrt{d}} \leq \mu\sqrt{\eta} \quad (10)$$

$$\text{where } \mu = \sqrt{\frac{\sum_{l>0} (\alpha^l)^2}{\alpha^0\alpha^1}}.$$

From (8) we see that standard networks, which have highly nonlinear loss landscapes, will have a small maximal distortion ratio. However, robust models have a smoother loss landscape (see Figure 3) and so the gradient direction changes occur less often during the attack, leading to higher distortions as demonstrated in Figure 1. Theorem 2 tells us that this high distortion results in LMO iterates that are tightly concentrated at the corners of the the ℓ_∞ ball. Further, the initial FW step is a strong near-optimal adversarial perturbation, which implies very small variation in the signed gradients near the corner point, $\text{sgn}(\nabla_x \mathcal{L}(x, y))$, and indicates that the variation in the direction of the gradient (if not its magnitude) is small.

The proofs of Proposition 1, Theorem 1 and 2 are in the supplementary, in addition to distortion bounds in the ℓ_2 norm case that depend on the local Lipschitz constant of the loss.

3.3 Convergence Analysis

Loss functions $\mathcal{L}(x + \delta, y)$ in deep neural networks are non-convex in general. For a targeted attack that aims to fool the classifier to predict a specific label, without loss of generality, we seek to minimize the loss $f(\delta) = \mathcal{L}(x + \delta, y')$ over a ℓ_p constraint set. The untargeted case follows similarly.³ For general non-convex constrained optimization, the Frank-Wolfe gap given by (5) is non-negative in general and zero at stationary points. The convergence of FW on non-convex functions has been studied in Lacoste-Julien [2016] and recently improved for strongly convex constraints in Rector-Brooks et al. [2019].

Assumption 1. *The function f has L -Lipschitz continuous gradients on $B_p(\epsilon)$, i.e., $\|\nabla f(u) - \nabla f(v)\| \leq L\|u - v\|, \forall u, v \in B_p(\epsilon)$.*

Assumption 2 is a standard assumption for the non-convex setting and has been made in several works Lacoste-Julien [2016], Chen et al. [2020]. A recent study Santurkar et al. [2018] shows that the batch normalization layer used in modern neural networks makes the loss much smoother. Other recent works Allen-Zhu et al. [2019], Zou and Gu [2019], Cao and Gu [2020] showed that the loss is semi-smooth for overparameterized DNNs. Furthermore, the process of adversarial training smooths the loss landscape in comparison to standard models significantly as Fig. 3 illustrates and other works have noted this phenomenon as well Moosavi-Dezfooli et al. [2019], Qin et al. [2019].

Given Assumption 2 and the compactness of the constraint sets, all limit points of FW are stationary points Bertsekas [1999]. The convergence rate of FW to a stationary point for optimization over arbitrary convex sets was first shown in Lacoste-Julien [2016] given by

$$\min_{1 \leq s \leq t} g(\delta_s) \leq \frac{\max\{2h_0, L \text{ diam}(B)\}}{\sqrt{t+1}}$$

where $h_0 = f(\delta_0) - \min_{\delta \in B(\epsilon)} f(\delta)$ is the initial global suboptimality. It follows that larger ϵ imply a larger diameter and more iterations may be needed to converge⁴. This result implies that an approximate stationary point can be found

³For untargeted attacks, $\min_{\delta \in B(\epsilon)} -\mathcal{L}(x + \delta, y)$ is considered and the FW gap becomes (5).

⁴The diameter of ℓ_2 ball is 2ϵ and for the ℓ_∞ ball $2\epsilon\sqrt{d}$.

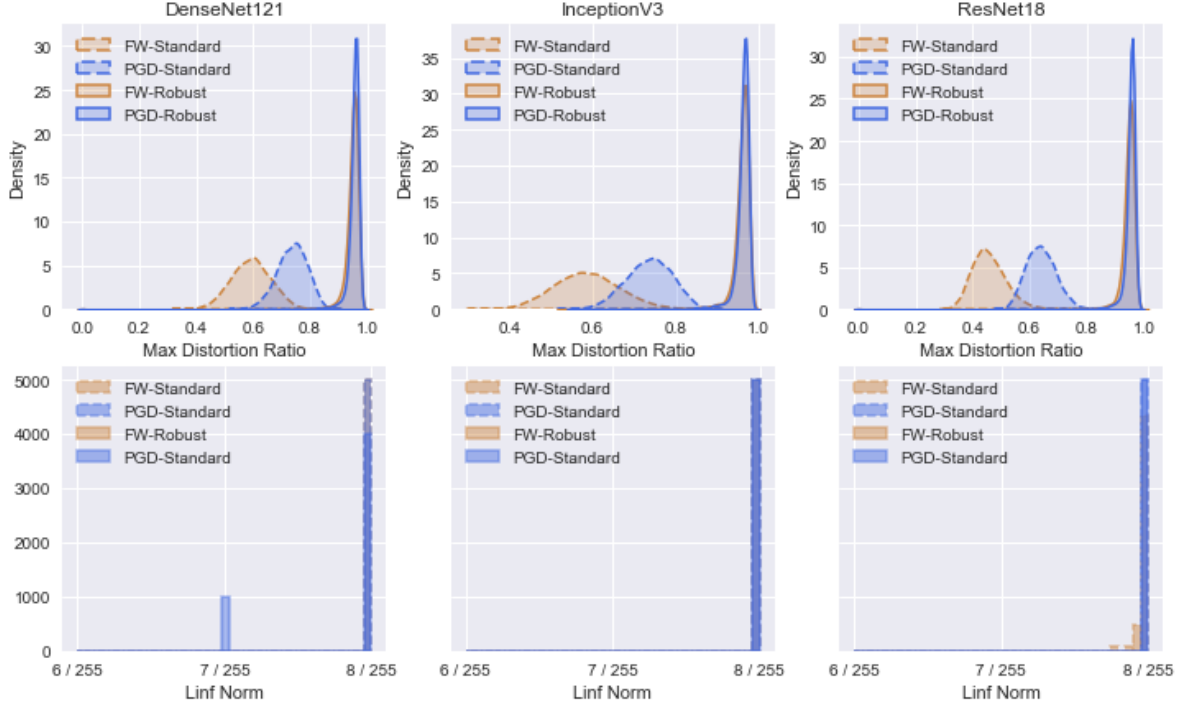


Figure 1: ℓ_∞ attacks using FW(20) and PGD(20) with $\epsilon = 8/255$ against standard (dashed) and robust (solid) models across three architectures. Kernel density estimates of the distribution of $\|\delta\|_2/(\epsilon\sqrt{d})$ (first row) and histogram of the ℓ_∞ norm of the attacks (second row).

with gap less than ϵ_0 in at most $O(1/\epsilon_0^2)$ iterations. Theorem 4 in Rector-Brooks et al. [2019] shows that for smooth non-convex functions over strongly convex constraint sets, FW yields an improved convergence rate $O(\frac{1}{t})$, which importantly does not hold for the ℓ_∞ constraint.

3.4 Algorithm

Algorithm 1 illustrates the Frank-Wolfe adversarial training method. The loss gradient is computed at each Frank-Wolfe iteration k , and the solution to the LMO $\bar{\delta}$ is given by (6). Then the adversarial perturbation δ is updated by taking a step along the direction $\bar{\delta} - \delta$. Once the adversarial examples are obtained, the model parameters θ are updated using a gradient-based optimizer (e.g. SGD).

Each step in the inner maximization based on the Frank-Wolfe procedure requires a forward-backward pass to evaluate $\nabla \mathcal{L}(\cdot)$, similarly to PGD. Thus $O(KN_w)$ time is needed for K steps of FW where N_w denotes the number of network parameters. After computing the adversarial direction δ^* , the gradient-based optimizer incurs an additional cost of $O(N_w)$ for all methods to update model parameters.

Algorithm 1 Frank-Wolfe Adversarial Training

Input: Network f_θ , Training data \mathcal{D} , Training epochs T , max number of steps K , batch size $|B|$, maximum perturbation ϵ , constant $c \geq 1$, learning rate schedule η_t .

Result: Robust model θ .

```

for  $t = 0$  to  $T - 1$  do
  for each batch  $(x, y) \sim \mathcal{D}$  do
    Initialize  $\delta = 0$ 
    while  $k < K$  do
       $\gamma = c/(c + k)$ 
       $\bar{\delta} = \epsilon \phi_p(\nabla_\delta \mathcal{L}(f_\theta(x + \delta), y))$ 
       $\delta = \delta + \gamma(\bar{\delta} - \delta)$ 
    end while
     $\theta = \theta - \eta_t \frac{1}{|B|} \sum_{i \in B} \nabla_\theta \mathcal{L}(f_\theta(x_i + \delta_i), y_i)$ 
  end for
end for

```

4 Counterfactual Explanations

The framework of counterfactual explanation aims to explain individual model predictions by looking for the closest image from the original that will change the prediction Wachter et al. [2018]. Closely related explanation methods includes contrastive ones that describe how features will change the prediction if absent or present Liao et al. [2020].

To this end, we seek to generate visual counterfactuals in the image space by constraining the change in the original image. Our framework is inspired by robust feature manipulation Tsipras et al. [2019] and the connection between the formulation of finding counterfactuals (4) and computing adversarial perturbations (11) Wachter et al. [2018], Sharma et al. [2020]. As the network’s prediction changes, class-specific features are expected to emerge. Standard models do not achieve this as they make use of predictive but non-robust features and decisions are changed by imperceptible perturbations. Therefore, we consider explaining decisions of robust models that have shown to have generative properties Tsipras et al. [2019], Santurkar et al. [2019].

Suppose we have $(x, y) \sim \mathcal{D}$, counterfactual images are generated to explain model predictions as defined by the optimization problems

$$\delta_{\max} = \underset{\delta \in B_p(\epsilon)}{\operatorname{argmax}} \mathcal{L}(x + \delta, y), \quad \delta_{\min} = \underset{\delta \in B_p(\epsilon)}{\operatorname{argmin}} \mathcal{L}(x + \delta, y), \quad (11)$$

we optimize the loss over a ℓ_p ball of radius ϵ to ensure that the modified example $x + \delta$ remains close to the original example x . C&W or DeepFool objectives may also be used in (11) but we found the loss yields more natural visual counterfactuals. For ℓ_2 counterfactual perturbations δ are dense, and sparse counterfactual perturbations can be obtained by optimizing the loss using the sparsity-inducing ℓ_1 norm instead. For correct predictions, δ_{\max} constructs a counterfactual image to explain how the correct prediction changes to an incorrect one, while δ_{\min} changes features to increase the confidence of the correct class. On the other hand, for incorrect predictions, δ_{\max} answers the counterfactual question of how features change to justify the incorrect label, and δ_{\min} shows feature changes to correct the error.

5 Experimental Results

We evaluate the performance of our proposed FW-AT against standard training, and PGD-AT Madry et al. [2018]. All networks were trained by fine-tuning a standard model.

5.1 Implementation

The models, training, and evaluation routines for our experiments were performed using the robustness library from Engstrom et al. [2019] which we modified to add the FW-AT method and support the SVHN dataset. Experiments were run on 2 Volta V100 GPUs. Hyperparameters for FW-AT were tuned to $c = 2$ with the goal of achieving near the adversarial accuracy of PGD-AT with step size $\alpha = 2.5\epsilon/K$ for $K = 10$ steps as this was the default setting in Engstrom et al. [2019]. Specifics can be found in the supplementary material.

Method	Clean	PGD(20)	PGD(100)	Square
FW-AT/ $c = 2$	84.37	47.86	47.22	53.10
FW-AT/ $c = 3$	84.19	48.02	47.61	53.50
FW-AT/ $c = 4$	84.16	48.04	47.43	52.50
FW-AT/ $c = 5$	84.16	48.34	47.84	53.20
FW-AT/ $c = 6$	84.09	47.80	47.33	52.90

Table 1: Model accuracy on CIFAR10 test set for FW(10)-AT ℓ_∞ robust networks trained for various step size hyperparameters on ResNet18 architecture. White-box PGD UL attacks and black-box Square attacks (1000 ex) at $\epsilon = 8/255$.

Method	Clean	UL	TL	UM	TM
Standard	94.54	1.37	15.62	1.88	16.82
FW(10)-AT	89.41	65.62	85.12	65.92	84.49
PGD(10)-AT	89.46	65.44	84.97	65.72	83.94

(a) ℓ_2 adversarial PGD(20) attacks with loss / margin at $\epsilon = 0.5$

Method	Clean	UL	TL	UM	TM
Standard	94.54	0.01	11.10	0.01	11.49
FW(10)-AT	84.37	47.86	74.37	46.56	72.41
PGD(10)-AT	84.12	47.75	75.30	46.83	72.45

(b) ℓ_∞ adversarial PGD(20) attacks with loss / margin at $\epsilon = 8/255$

Table 2: Model accuracy on CIFAR-10 test set against various attacks on ResNet18 architecture. Our proposed FW-AT method has high robustness similar to PGD-AT.

5.2 Adversarial Robustness

To test the robustness of our network, we consider a variety of adversarial attacks, including white-box untargeted and targeted attacks towards a random class $r \sim \mathcal{U}(\{1, \dots, K\} \setminus y)$. The white-box setup considers attack techniques that have full access to the model parameters and are constrained by the same maximum perturbation size ϵ . The classification margin is defined as $M(x, y) = \log p_y(x) - \max_{j \neq y} \log p_j(x)$. The following white-box attacks are used for evaluating adversarial robustness:

- (UL) **Untargeted-loss:** $\max_{\delta \in B(\epsilon)} \mathcal{L}(x + \delta, y)$
- (TL) **Random Targeted-loss:** $\max_{\delta \in B(\epsilon)} \mathcal{L}(x + \delta, r)$
- (UM) **Untargeted-margin:** $\min_{\delta \in B(\epsilon)} M(x + \delta, y)$
- (TM) **Random Targeted-margin:** $\max_{\delta \in B(\epsilon)} M(x + \delta, r)$

The performance metric used is the accuracy on the test set after the attack is applied (adversarial accuracy). In general untargeted attacks are stronger than targeted ones. Table 2 reports robustness results on CIFAR-10 for the specific attacks in the ℓ_2 and ℓ_∞ cases for a ResNet18 architecture. FW-AT achieves robustness competitive with PGD-AT for untargeted and targeted attacks. Similar trends are shown on SVHN in the supplemental material (also Table 3). Additional results are shown on DenseNet121, InceptionV3, and ResNet50 architectures in Table 5.

A sensitivity analysis is presented in Table 1 to study the effect of step size on robustness of FW-AT that shows FW-AT is not sensitive to step size parameter selection.

5.3 Evaluating Gradient Masking

We evaluate gradient masking by following a similar evaluation protocol as in Moosavi-Dezfooli et al. [2019] inspired by Uesato et al. [2018]. Table 3 shows that our method achieves similar adversarial accuracy on the test set when evaluated against PGD attacks of increasing strength. Thus increasing the attack’s complexity does not deteriorate the adversarial accuracy significantly.

In the black-box setting, attacks have access to the inputs and output logits (partial or full) only. Our models are evaluated against black-box gradient-free methods that repeatedly perform queries to construct adversarial images including SimBA Guo et al. [2019] and Square attack Andriushchenko et al. [2020]. Attack parameters can be found in the supplementary material. Table 4 contains the adversarial accuracy obtained under PGD(100) white-box attack

Method	Clean	PGD(20)	PGD(100)
CIFAR10/ ℓ_2 FW-AT	89.41	65.62	65.29
CIFAR10/ ℓ_2 PGD-AT	89.46	65.44	65.16
CIFAR10/ ℓ_∞ FW-AT	84.37	47.86	47.22
CIFAR10/ ℓ_∞ PGD-AT	84.12	47.75	47.21
SVHN/ ℓ_2 FW-AT	94.63	70.02	69.51
SVHN/ ℓ_2 PGD-AT	95.00	69.98	69.45
SVHN/ ℓ_∞ FW-AT	94.23	57.36	56.42
SVHN/ ℓ_∞ PGD-AT	94.41	54.46	52.88

Table 3: Model accuracy on CIFAR-10 (top set) and SVHN (bottom set) test set for untargeted loss (UL) adversarial ℓ_2 (and ℓ_∞) PGD attacks at $\epsilon = 0.5$ (and $\epsilon = 8/255$) for ℓ_2 (and ℓ_∞) robust networks trained on ResNet18 architecture. For evaluation, the step size was set to $\alpha = 2\epsilon/10$ ($= 0.1$ for ℓ_2 and $= 1.6/255$ for ℓ_∞). Our proposed method, FW-AT, achieves high adversarial accuracy and resistance to gradient masking similar to PGD-AT.

Method	PGD(100)	SimBA	Square
CIFAR10/ ℓ_∞ FW-AT	50.40	70.60	53.10
CIFAR10/ ℓ_∞ PGD-AT	49.10	70.40	52.20
SVHN/ ℓ_∞ FW-AT	55.50	81.40	54.20
SVHN/ ℓ_∞ PGD-AT	55.00	79.60	52.00

Table 4: Model accuracy on white-box PGD(100) and black-box (SimBA, Square) attacks on CIFAR10/SVHN test subset (1000 examples) for ℓ_∞ robust networks trained on ResNet18 architecture. The ℓ_∞ attacks use $\epsilon = 8/255$. FW-AT maintains strong robustness against a variety of black-box attacks.

and several black-box attacks against ℓ_∞ -robust FW and PGD models. It is evident that the proposed FW-AT defense achieves similar robustness to PGD-AT.

Figure 2 compares the margin computed using Square attack and PGD(100) attack for a large batch of test points. It is observed that both methods lead to a similar adversarial loss except on a very small subset of points (48 out of 1000) for FW-AT which improves upon the number of red points for PGD-AT (65 out of 1000). Here, the adversarial loss is the classification margin that captures confidence, and is positive for correct predictions and negative for misclassifications. The results in Tables 3, 4 and Fig. 2 further verify that FW-AT improves the true robustness and does not suffer from grading masking or obfuscation.

Adversarial accuracy results for a variety of additional architectures including DenseNet121, InceptionV3, and ResNet50, are shown in Table 5. In all experiments FW-AT achieves robustness competitive with PGD-AT building upon our empirical results on ResNet18.

5.4 Loss Landscape

It has been shown experimentally that many robust models, including AT and the geometric-regularization methods (e.g. CURE), have more regular loss landscapes than their non-robust counterparts Lyu et al. [2015], Ros and Doshi-Velez [2018], Moosavi-Dezfooli et al. [2019], Qin et al. [2019]. Figure 3 shows sample loss surfaces for a standard model, PGD(10)-AT, and FW(10)-AT. The white circle denotes the original image, and the red circle denotes the ℓ_∞ adversarial perturbation at $\epsilon = 8/255$. One direction is the adversarial perturbation and the other is a random orthogonal direction. The loss surface of standard models is highly non-linear and the loss varies significantly in this small neighborhood, with the largest variation occurs in the adversarial direction. Figure 3 (b) and (c) demonstrate that robust models offer more resistance to such local loss variation and the variation is primarily in the direction of the adversarial attack. These results suggest high resistance to gradient obfuscation.

5.5 Counterfactual Explanations

Figure 4 shows examples of the counterfactual explanations for two sample images from the CIFAR10 test set. The images' target labels are ship and airplane. The model correctly classified the ship and misclassified the airplane as a ship. The explanations are generated by solving (11) in the dense case we restrict perturbations to the ℓ_2 ball of radius 2 and use FW(20) and for the sparse case we restrict to the ℓ_1 ball of radius of $255/4$ and use FW(768). The high number of steps is necessary as each Franke-Wolfe step in the ℓ_1 optimization modifies at most one pixel at a time. FW(768) can modify at most 25% of the total pixels. Indeed the ℓ_1 perturbations are sparse which can allow for more focused interpretations of the prediction, offering an advantage over PGD since projection onto the ℓ_1 ball lacks a closed-form.

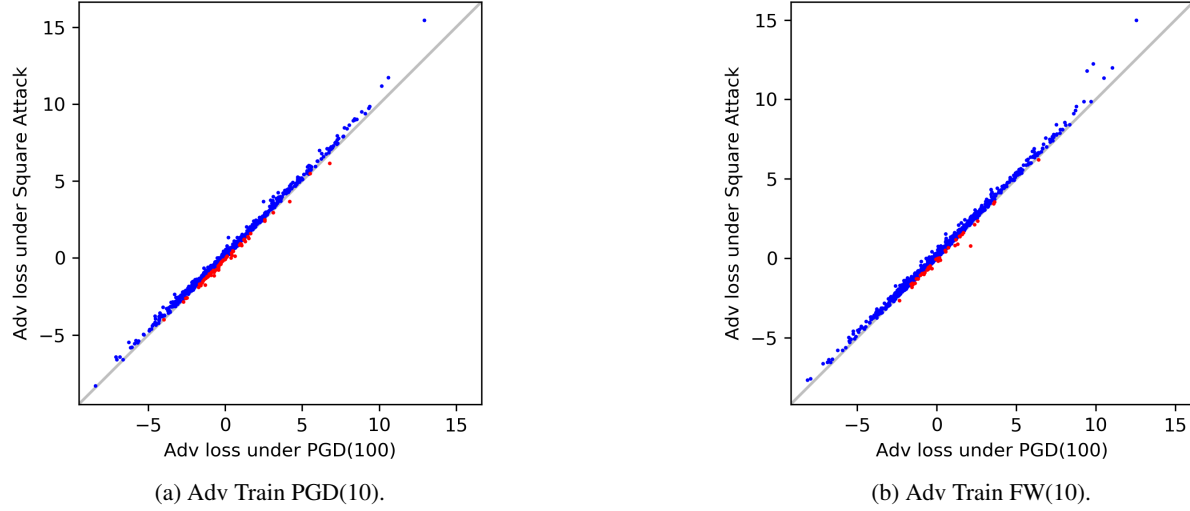


Figure 2: Gradient masking analysis for CIFAR10 PGD-AT and FW-AT ℓ_∞ robust networks trained on ResNet18 architecture. Adversarial loss (classification margin) was computed with black-box Square Attack for the y-axis and white-box PGD(100) attack at $\epsilon = 8/255$ for x-axis on a set of 1000 test points. Points near the line $y = x$ indicate both types of attacks found similar adversarial perturbations, while points below the line shown in red imply that Square Attack identified stronger attacks than PGD. FW-AT exhibits a higher resistance to gradient masking.

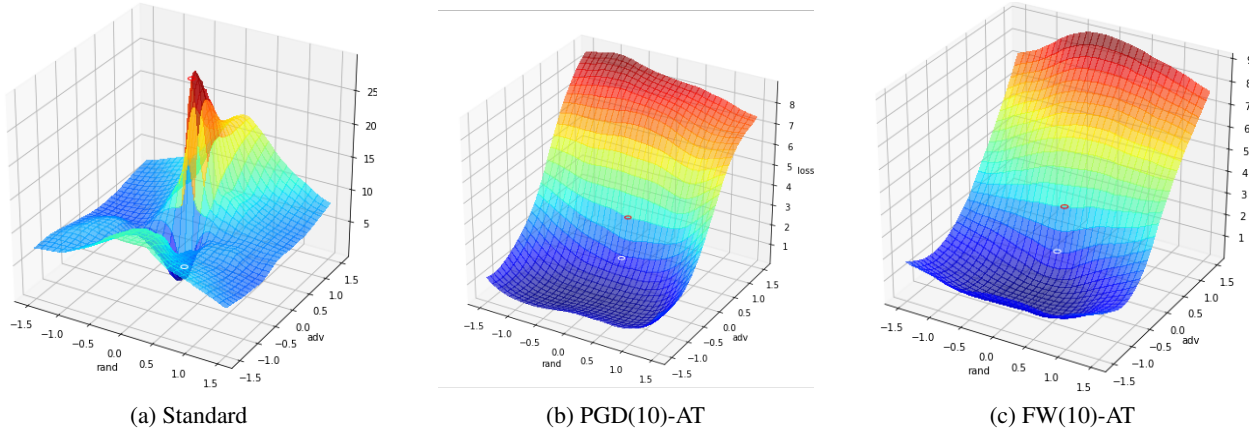


Figure 3: Loss landscapes for an image from CIFAR10 test set. ResNet18 architecture. Standard models have highly non-linear loss surfaces as opposed to robust models which have smoother landscapes.

(Ar) Method	Clean	PGD(20)	PGD(100)	Square
(D) FW-AT	84.17	49.27	48.77	54.50
(D) PGD-AT	84.18	48.46	47.94	53.60
(I) FW-AT	85.45	47.40	46.88	53.00
(I) PGD-AT	85.52	47.50	47.10	53.30
(R) FW-AT	84.98	48.90	48.26	54.60
(R) PGD-AT	85.20	49.29	48.68	53.60

Table 5: Model accuracy on CIFAR10 test set for FW(10)-AT and PGD(10)-AT ℓ_∞ robust networks trained on DenseNet121 (D), InceptionV3 (I) and ResNet50 (R) architectures. white-box PGD(20) UL attacks and black-box Square attacks (1000 examples) at $\epsilon = 8/255$.

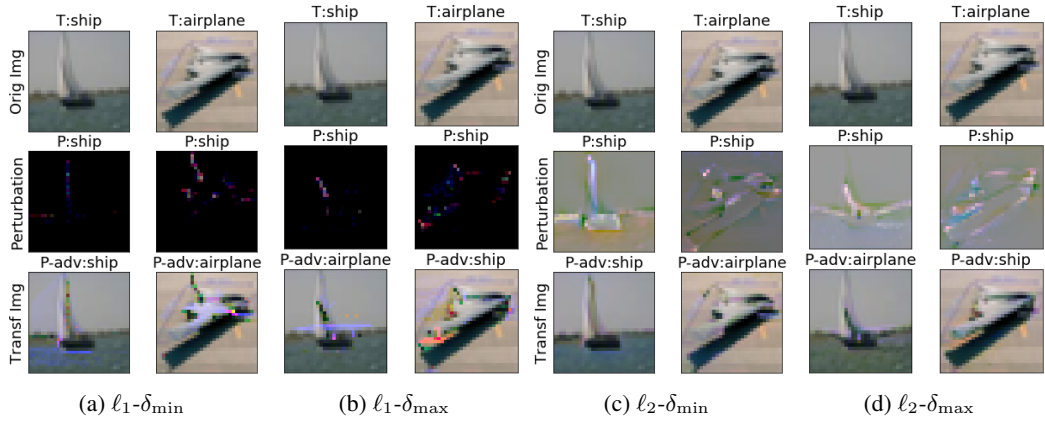


Figure 4: Sparse (a) and (b) and dense (c) and (d) counterfactual explanations via perturbations generated using (11). ℓ_1 perturbations modified at most 25% of pixels with FW(768) and ℓ_2 perturbations were performed with FW(20) and $\epsilon = 2$. Images are titled with their target label (T), the model’s prediction (P), and its adversarial prediction (P-adv).

Consider the minimization perturbations (Figures 4a and 4c) for the correctly classified ship image (first column). The δ_{\min} perturbations show features that the model believes should be emphasized to become more confident in its correct prediction. The perturbations focus on the sail and seem to emphasize the water in the image. For the second column the δ_{\min} displays features that need to be added to correct the model’s misclassification of the airplane as a ship and the perturbations focus on the cockpit of the airplane and seem to add more of a traditional tail to the image.

The maximization perturbations (Figures 4b and 4d) for the correctly classified ship image (first column) show features of the image that could be emphasized to make a mistake. They emphasize the horizon to form wings and the mast to form a tail. For the second column δ_{\min} shows what features led to the model’s misclassification of the airplane as a ship. The sparse perturbations emphasize the wing tip while the ℓ_2 model seems to blur the boundary overall making a perturbation which itself appears to be a ship.

6 Conclusion

One of the most effective defenses against adversarial perturbations is adversarial training (AT) under which networks are trained to be robust against worst-case ℓ_p -norm perturbations computed using projected gradient descent (PGD). Frank-Wolfe adversarial training (FW-AT) is presented and an interesting phenomenon is shown for robust models; higher ℓ_2 distortions are obtained than standard ones despite achieving nearly the same ℓ_∞ distortion. To explain this, distortion guarantees are derived to relate local loss geometry to the magnitude of FW adversarial perturbation for the ℓ_∞ case. FW-AT is empirically demonstrated to have high robustness on par with PGD-AT against strong white-box and black-box attacks, and offers strong resistance to gradient obfuscation. Sparse visual counterfactual explanations are generated using FW optimization.

Method	Clean	UL	TL	UM	TM
Standard	94.54	1.37	15.62	1.88	16.82
Gradient Reg	89.16	29.90	70.45	30.91	66.43
CURE	88.27	53.43	82.01	53.13	79.49
FW(10)-AT	89.41	65.62	85.12	65.92	84.49
PGD(10)-AT	89.46	65.44	84.97	65.72	83.94

(a) ℓ_2 adversarial PGD(20) attacks with loss / margin at $\epsilon = 0.5$

Method	Clean	UL	TL	UM	TM
Standard	94.54	0.01	11.10	0.01	11.49
Gradient Reg	82.51	4.79	37.42	6.03	32.25
CURE	81.06	20.73	59.99	21.33	54.36
FW(10)-AT	84.37	47.86	74.37	46.56	72.41
PGD(10)-AT	84.12	47.75	75.30	46.83	72.45

(b) ℓ_∞ adversarial PGD(20) attacks with loss / margin at $\epsilon = 8/255$

Table 6: Model accuracy on CIFAR-10 test set against various attacks. Our proposed method FW-AT outperforms prior gradient and curvature regularization methods and is competitive with PGD-AT.

Acknowledgements

Research was sponsored by the United States Air Force Research Laboratory and the United States Air Force Artificial Intelligence Accelerator and was accomplished under Cooperative Agreement Number FA8750-19-2-1000. The views and conclusions contained in this document are those of the authors and should not be interpreted as representing the official policies, either expressed or implied, of the United States Air Force or the U.S. Government. The U.S. Government is authorized to reproduce and distribute reprints for Government purposes notwithstanding any copyright notation herein.

Appendix

Training Details

Training. All robust models were trained starting from a pre-trained standard model. Training was performed for 61 epochs. A SGD optimizer was used with initial learning rate 0.01 and decayed to 0.001 after 50 epochs. The best model that achieves the highest adversarial accuracy on a heldout set is chosen in all experiments.

Hyperparameters

White box attacks. Our experiments are based on K -step PGD attacks with step size tuned to $\alpha = 2.5\epsilon/10$. This is equal to $\alpha = 0.125$ for the ℓ_2 norm and $\alpha = 2/255$ for the ℓ_∞ norm.

Black box attacks. The parameters used for the black-box attacks are the following: SimBA $T = 200$ iterations, $\epsilon = 0.2$, Square attack $T = 5000$ steps, $p_{init} = 0.8$, $\epsilon = 8/255$.

White Box Robustness Results

Tables 6 and 7 show the adversarial accuracy of FW-AT on CIFAR-10 and SVHN respectively, in comparison to standard training, PGD-AT Madry et al. [2018], gradient regularization (Grad-Reg) Ros and Doshi-Velez [2018], and curvature regularization (CURE) Moosavi-Dezfooli et al. [2019]. All networks were trained by fine-tuning the standard model. It is observed that FW-AT achieves similar robustness as PGD-AT on both datasets.

Proof of Proposition 1

Proof. The LMO solution is given by $\bar{\delta}^k = \epsilon \phi_p(\nabla_\delta \mathcal{L}(x + \delta^k, u))$ and the update becomes

$$\begin{aligned} \delta^{k+1} &= \delta^k + \gamma^k (\bar{\delta}^k - \delta^k) \\ &= (1 - \gamma^k) \delta^k + \gamma^k \epsilon \phi_p(\nabla \mathcal{L}(x + \delta^k, y)) \end{aligned}$$

Method	Clean	UL	TL	UM	TM
Standard	97.04	9.77	30.09	10.00	30.54
Gradient Reg	95.00	46.39	76.48	47.15	74.43
CURE	94.68	63.78	86.29	63.33	84.66
FW(10)-AT	94.63	70.03	88.36	68.54	87.15
PGD(10)-AT	95.00	69.98	88.60	68.96	86.97

(a) ℓ_2 adversarial PGD(20) attacks with loss / margin at $\epsilon = 0.5$

Method	Clean	UL	TL	UM	TM
Standard	97.04	0.51	12.75	0.52	13.36
Gradient Reg	91.42	6.10	29.01	7.13	26.04
CURE	91.61	30.36	59.25	29.79	54.69
FW(10)-AT	94.23	57.36	79.28	54.42	75.29
PGD(10)-AT	94.41	54.46	77.33	53.03	73.69

(b) ℓ_∞ adversarial PGD(20) attacks with loss / margin at $\epsilon = 8/255$

Table 7: Model accuracy on SVHN test set against various attacks. Our proposed method FW-AT outperforms prior gradient and curvature regularization methods and is competitive with PGD-AT.

Using induction on this relation yields after K steps:

$$\delta^K = \delta^0 \prod_{l=0}^{K-1} (1 - \gamma^l) + \epsilon \sum_{l=0}^{K-1} \gamma^l \prod_{i=l+1}^{K-1} (1 - \gamma^i) \phi_p(\nabla_\delta \mathcal{L}(x + \delta^k, y)) \quad (12)$$

where δ^0 is the initial point which affects both terms in (12) and $\gamma^k = c/(c+k)$ for $k \geq 0$. Since $\gamma^0 = 1$, the first term vanishes and (12) simplifies to

$$\delta^K = \epsilon \sum_{l=0}^{K-1} \alpha^l \phi_p(\nabla_\delta \mathcal{L}(x + \delta^l, y)) \quad (13)$$

where the coefficients are

$$\alpha^l = \gamma^l \prod_{i=l+1}^{K-1} (1 - \gamma^i) \quad (14)$$

Since $\gamma^l \in [0, 1]$, it follows that $\alpha^l \in [0, 1]$. Induction on (14) yields that $\sum_{l=0}^{K-1} \alpha^l = 1$. Furthermore, $\alpha^l \leq \alpha^{l+1}$ follows from:

$$\begin{aligned} \alpha^l &\leq \alpha^{l+1} \\ \Leftrightarrow \gamma^l (1 - \gamma^{l+1}) &\leq \gamma^{l+1} \\ \Leftrightarrow \frac{c}{c+l} \left(1 - \frac{c}{c+l+1}\right) &\leq \frac{c}{c+l+1} \\ \Leftrightarrow \frac{l+1}{c+l} &\leq 1 \\ \Leftrightarrow 1 &\leq c \end{aligned}$$

Thus, the sequence α^l is non-decreasing in l . Since the coefficients sum to unity, (13) is in the convex hull of the generated LMO sequence $\{\phi_p(\nabla_\delta \mathcal{L}(x + \delta^l)) : l = 0, \dots, K-1\}$. \square

Proof of Theorem 1

Proof. From Proposition 1, we obtain the following decomposition of the adversarial perturbation:

$$\delta^K = \epsilon \sum_{l=0}^{K-1} \alpha^l \text{sgn}(\nabla_\delta \mathcal{L}(x + \delta^l, y))$$

To bound the magnitude of the adversarial perturbation, we have

$$\|\delta^K\|_2 = \sqrt{\|\delta^K\|_2^2} = \epsilon \sqrt{\left\| \sum_l \alpha^l s^l \right\|_2^2}$$

where we use the shorthand notation $s^l = \text{sgn}(\nabla_\delta \mathcal{L}(x + \delta^l, y))$. The squared ℓ_2 norm in the above is bounded as:

$$\begin{aligned}
\left\| \sum_l \alpha^l s^l \right\|_2^2 &= \sum_l \sum_j \alpha^l \alpha^j \langle s^l, s^j \rangle \\
&= \sum_l (\alpha^l)^2 \|s^l\|_2^2 + \sum_{l \neq j} \alpha^l \alpha^j \|s^l\|_2 \|s^j\|_2 \cos \beta^{lj} \\
&= d \left(\sum_l (\alpha^l)^2 + \sum_{l \neq j} \alpha^l \alpha^j \cos \beta^{lj} \right) \\
&= d \left(\sum_l (\alpha^l)^2 + \sum_{l \neq j} \alpha^l \alpha^j - \sum_{l \neq j} \alpha^l \alpha^j (1 - \cos \beta^{lj}) \right) \\
&= d \left(1 - \sum_{l \neq j} \alpha^l \alpha^j (1 - \cos \beta^{lj}) \right) \\
&= d \left(1 - 2 \sum_{l < j} \alpha^l \alpha^j (1 - \cos \beta^{lj}) \right)
\end{aligned}$$

where we used $\|s^l\|_2 = \sqrt{d}$ and from Proposition 1 $(\sum_l \alpha^l)^2 = 1$. The final step follows from symmetry. This concludes the proof. \square

Proof of Theorem 2

Proof. From Theorem 1 and the lower bound on the distortion, it follows that:

$$\sum_{l < j} \alpha^l \alpha^j (1 - \cos \beta^{lj}) \leq \eta/2$$

Lower-bounding the left-hand side of the above:

$$\min_{l < j} \{\alpha^l \alpha^j\} \sum_{l < j} (1 - \cos \beta^{lj}) \leq \eta/2 \quad (15)$$

Proposition 1 implies due to the non-decreasing sequence α^i ,

$$\min_{l < j} \{\alpha^l \alpha^j\} = \alpha^0 \alpha^1$$

Furthermore, letting $s^i = \text{sgn}(\nabla \mathcal{L}(x + \delta^i, y))$ and expanding the squared difference of signed gradients:

$$\begin{aligned}
\|s^l - s^j\|_2^2 &= \|s^l\|_2^2 + \|s^j\|_2^2 - 2 \langle s^j, s^l \rangle \\
&= \|s^l\|_2^2 + \|s^j\|_2^2 - 2 \|s^j\|_2 \|s^l\|_2 \cos \beta_{lj} \\
&= d + d - 2d \cos \beta^{lj} \\
&= 2d(1 - \cos \beta^{lj})
\end{aligned}$$

Upon re-arrangement,

$$\begin{aligned}
1 - \cos \beta_{lj} &= \frac{\|s^l - s^j\|_2^2}{2d} = \frac{1}{2d} \sum_{i=1}^d (s_i^l - s_i^j)^2 \\
&= \frac{1}{2d} \sum_{i=1}^d 4 \cdot \mathbb{1}_{\{s_i^l \neq s_i^j\}} \\
&= \frac{2}{d} n^{lj}
\end{aligned}$$

where $n^{lj} = \sum_{i=1}^d \mathbb{1}_{\{s_i^l \neq s_i^j\}}$ is the number of sign changes between the gradients $\nabla_\delta \mathcal{L}(x + \delta^l, y)$ and $\nabla_\delta \mathcal{L}(x + \delta^j, y)$. Using this expression and simplifying (15), we obtain (9)

$$\sum_{l < j} \frac{n^{lj}}{d} \leq \frac{\eta}{4\alpha^0 \alpha^1}$$

This concludes the first part. For the second part (10), we have by the triangle inequality:

$$\begin{aligned}
\|\delta^k - \epsilon \text{sgn}(\nabla_x \mathcal{L}(x, y))\|_2 &= \|\epsilon \sum_{l=0}^{K-1} \alpha^l s^l - \epsilon s^0\|_2 \\
&= \|\epsilon \sum_l \alpha^l s^l - \sum_l \alpha^l \epsilon s^0\|_2 \\
&= \epsilon \left\| \sum_l \alpha^l (s^l - s^0) \right\|_2 \\
&\leq \epsilon \sum_{l>0} \alpha^l \|s^l - s^0\|_2
\end{aligned} \tag{16}$$

Using Cauchy-Schwarz inequality, we obtain:

$$\begin{aligned}
\sum_{l>0} \alpha^l \|s^l - s^0\|_2 &\leq \sqrt{\sum_{l>0} (\alpha^l)^2} \sqrt{\sum_{l>0} \|s^l - s^0\|_2^2} \\
&= \sqrt{\sum_{l>0} (\alpha^l)^2} \sqrt{\sum_{l>0} 4n^{lj}} \\
&\leq \sqrt{\sum_{l>0} (\alpha^l)^2} \cdot 2 \sqrt{\sum_{l<j} n^{lj}} \\
&\leq \sqrt{\sum_{l>0} (\alpha^l)^2} \cdot 2 \sqrt{\frac{\eta d}{4\alpha^0 \alpha^1}} \\
&= \sqrt{\sum_{l>0} (\alpha^l)^2} \sqrt{\frac{\eta d}{\alpha^0 \alpha^1}}
\end{aligned} \tag{17}$$

where we used Proposition 1, the earlier relation $\|s^l - s^j\|_2^2 = 4n^{lj}$, and the upper bound on the number of sign changes (9). Combining (17) with (16), we obtain:

$$\|\delta^k - \epsilon \text{sgn}(\nabla_x \mathcal{L}(x, y))\|_2 \leq \epsilon \sqrt{\eta d} \sqrt{\frac{\sum_{l>0} (\alpha^l)^2}{\alpha^0 \alpha^1}}$$

This completes the proof. \square

Distortion Analysis for ℓ_2 Adversarial Training

For the case of ℓ_2 -adversarial training, the distortion bound (8) can be tied to the Lipschitz constant of the loss. Consider the following local smoothness condition.

Assumption 2. *The loss function $\mathcal{L}(x + \delta, y)$ has L -Lipschitz continuous gradients on $B_2(\epsilon)$,*

$$\|\nabla_\delta \mathcal{L}(x + u, y) - \nabla_\delta \mathcal{L}(x + v, y)\|_2 \leq L\|u - v\|_2, \tag{18}$$

for all u, v in the ball $B_2(\epsilon)$.

Assumption 2 is a standard assumption for the non-convex setting and has been made in several works Lacoste-Julien [2016], Chen et al. [2020]. A recent study Santurkar et al. [2018] shows that the batch normalization layer used in modern neural networks makes the loss much smoother. Other recent works Allen-Zhu et al. [2019], Zou and Gu [2019], Cao and Gu [2020] showed that the loss is semi-smooth for overparameterized DNNs. Furthermore, the process of adversarial training smooths the loss landscape in comparison to standard models significantly and other works have noted this phenomenon as well Moosavi-Dezfooli et al. [2019], Qin et al. [2019].

Theorem 3. *Let Assumption 2 hold. Consider the FW-AT Algorithm with step sizes $\gamma^k = c/(c + k)$ for some $c \geq 1$ and the ℓ_2 norm case. Let $\cos \beta^{lj}$ be the directional cosine between the gradients $\nabla_\delta \mathcal{L}(x + \delta^j, y)$ and $\nabla_\delta \mathcal{L}(x + \delta^l, y)$.*

Then, the following bound holds on the magnitude of the adversarial perturbation δ^K :

$$\|\delta^K\|_2 = \epsilon \sqrt{1 - 2 \sum_{l < j} \alpha^l \alpha^j (1 - \cos \beta^{lj})} \quad (19)$$

$$\geq \epsilon \sqrt{1 - L^2 \sum_{l < j} \frac{\alpha^l \alpha^j \|\delta^l - \delta^j\|_2^2}{\min_{i \in \{l, j\}} \|\nabla_{\delta} \mathcal{L}(x + \delta^i, y)\|_2^2}} \quad (20)$$

Proof. Following the proof of Theorem 1, we obtain (19). Let $s^l = \nabla_{\delta} \mathcal{L}(x + \delta^l, y) / \|\nabla_{\delta} \mathcal{L}(x + \delta^l, y)\|_2$. Using the relation $2(1 - \cos \beta^{lj}) = \|s^l - s^j\|_2^2$ in (19), we obtain:

$$\|\delta^K\|_2 = \epsilon \sqrt{1 - \sum_{l < j} \alpha^l \alpha^j \|s^l - s^j\|_2^2} \quad (21)$$

Then using Assumption 2, we obtain:

$$\begin{aligned} \|s^l - s^j\|_2 &= \left\| \frac{\nabla_{\delta} \mathcal{L}(x + \delta^l, y)}{\|\nabla_{\delta} \mathcal{L}(x + \delta^l, y)\|_2} - \frac{\nabla_{\delta} \mathcal{L}(x + \delta^j, y)}{\|\nabla_{\delta} \mathcal{L}(x + \delta^j, y)\|_2} \right\|_2 \\ &\leq \frac{\|\nabla_{\delta} \mathcal{L}(x + \delta^l, y) - \nabla_{\delta} \mathcal{L}(x + \delta^j, y)\|_2}{\min_{i \in \{l, j\}} \|\nabla_{\delta} \mathcal{L}(x + \delta^i, y)\|_2} \\ &\leq \frac{L \|\delta^l - \delta^j\|_2}{\min_{i \in \{l, j\}} \|\nabla_{\delta} \mathcal{L}(x + \delta^i, y)\|_2} \end{aligned}$$

Using this bound in (21) yields the lower bound (20). The proof is complete. \square

Theorem 3 implies that the smaller the Lipschitz constant L , the higher the ℓ_2 distortion associated with the adversarial perturbation. Thus, models with smaller loss curvature are expected to have large ℓ_2 distortions. This is in line with robust models which have been shown to have lower curvature than standard models Moosavi-Dezfooli et al. [2019].

Interpretability

We compare the quality of the saliency maps generated with a variety of regularized networks, in addition to adversarial perturbations that can serve as counterfactuals for explanations. Standard networks produce noisy saliency maps, as previously noted Etmann et al. [2019], and the higher level of robustness a network exhibits the more the network focuses on the object semantics as shown in Figure 5a. This is a good sign of lack of gradient obfuscation Qin et al. [2019]. Using ℓ_2 robust networks, the counterfactual images generated in Figure 5b by maximizing the loss align better with human perception for our method than for gradient and curvature regularized models.

q-Sparse ImageNet Counterfactuals

Here we provide additional examples of counterfactuals on ImageNet Deng et al. [2009]. An advantage of the counterfactual method is that it not only scales with, but improves when the number of classes and concepts increase. The higher resolution increases the computational overhead slightly, but also adds richness to the explanations. To generate these counterfactuals we used a ResNet50 network trained to be robust with respect to ℓ_2 adversarial attacks⁵.

Given data $(x, y) \sim D$, model f_{θ} , and model prediction \hat{y} , we consider two types of attacks.

Label Targeted

$$\delta^* = \underset{\delta \in B_p(\epsilon)}{\operatorname{argmin}} \mathcal{L}(f_{\theta}(x + \delta), y) \quad (22)$$

and prediction targeted

$$\delta^* = \underset{\delta \in B_p(\epsilon)}{\operatorname{argmin}} \mathcal{L}(f_{\theta}(x + \delta), \hat{y}) \quad (23)$$

Sparsity of explanations is a desirable property so one might consider ℓ_1 counterfactuals, particularly since FW can be used in the optimization without need for expensive projections. However, even with this non-projection advantage, the

⁵Models from: <https://github.com/MadryLab/robustness>

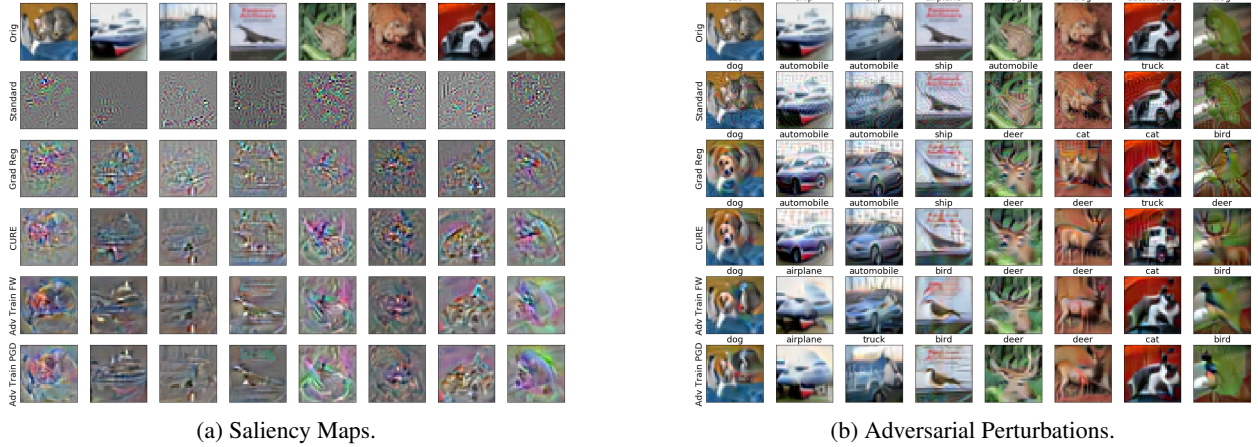


Figure 5: Saliency maps and PGD(20) untargeted adversarial attacks on the loss for sample examples from CIFAR-10 test set. FW-AT achieves more realistic-looking adversarial perturbations and improves saliency map quality.

LMO for ℓ_1 optimization only allows one pixel to be modified per FW step. Inspired by Kang et al. [2019] we modify ϕ_1 into $\phi_{1,q}$, where $\phi_{1,q}(x)_i = 1$ if $|x_i|$ is in the top q^{th} -percentile of $(|x_1|, \dots, |x_d|)$. The modified LMO is then scaled to remain in $B_1(\epsilon)$. The pseudo-code can be found in Algorithm 2. Though this is no longer an honest ℓ_1 adversarial attack it retains the desired sparsity as only $100 - q$ percent of the input pixels may be modified at each step. To choose our $\epsilon_0 = \epsilon\sqrt{d}$, where d is the dimension of the input, so that the attack contains attacks of ℓ_2 strength ϵ .

Algorithm 2 q-Sparse Counterfactual PseudoCode in Pytorch Style

Input: Network f_θ , input image x , target label y , max number of steps K , maximum perturbation ϵ , constant $c \geq 1$, and percentile q .

Result: Counterfactual δ .

Initialize $\delta = 0$

for $k < K$ **do**

$$\gamma = c/(c + k)$$

$$\bar{\delta} = 0$$

$$g = \nabla_\delta \mathcal{L}(f_\theta(x + \delta), y)$$

$$\text{top_q} = \text{torch.topk}(g.abs(), (1 - q) * \text{dim}(x))$$

$$\bar{\delta}[\text{top_q}] = \text{sgn}(g)$$

$$\bar{\delta} = \bar{\delta} / \|\bar{\delta}\|_1$$

$$\delta = \delta + \gamma(\bar{\delta} - \delta)$$

end for

Error Counterfactuals.

Figures 6a and 6b show counterfactual explanations for errors made by the model. The prediction targeted counterfactuals 6a answers the question:

Why did the model make this mistake?

For example in the first column the model mistakes a sidewinder snake for a horned viper. To become more confident in this error the model makes the spikes on the eyes of the sidewinder more pronounced, making it appear more like the horned viper. This suggests two things, firstly, that the model learned the characteristic that horned vipers have horn shaped eyes, and secondly, that the pointy eyes common in sidewinders confused the model. The second column suggests that the ships under the bridge were mistaken as pier pilings.

Figure 6b shows label targeted counterfactuals, which aim to answer the question:

What could have corrected this mistake?

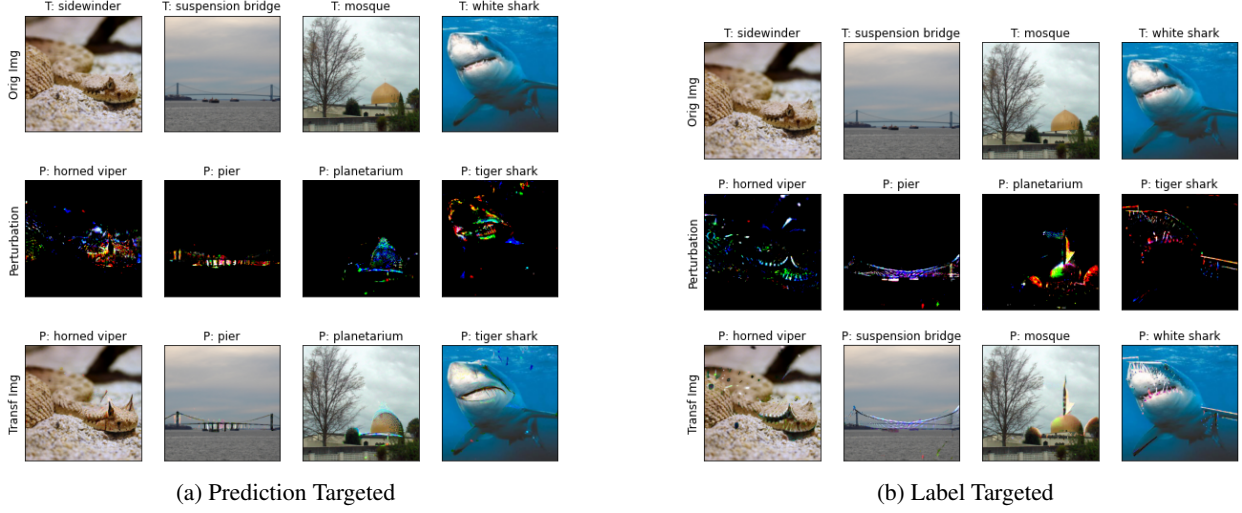


Figure 6: Prediction (a) and Label (b) targeted counterfactual explanations of errors using an ℓ_1 top-q attack with $q = 99\%$, $\epsilon = 10 * \sqrt{d}$, and 15 iterations. The Perturbations row has been magnified 10x for visibility

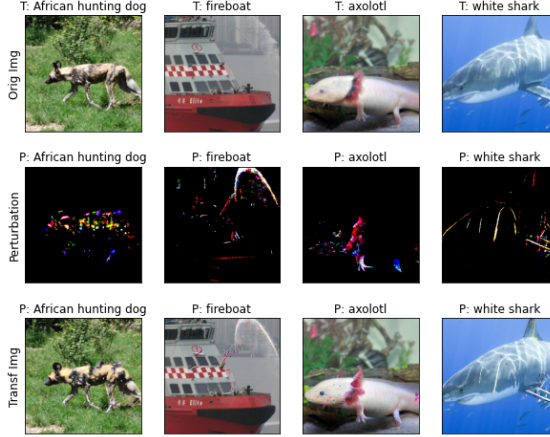


Figure 7: Prediction targeted counterfactual explanations of correct predictions using an ℓ_1 top-q attack with $q = 99\%$, $\epsilon = 10 * \sqrt{d}$, and 15 iterations. The Perturbations row has been magnified 10x for visibility

We see the model would have corrected its sidewinder prediction if the image had more pronounced splotch patterns common in sidewinder snakes and the suspension bridge prediction would have benefited from a more pronounced suspension cable. More interestingly is the third column where the model misidentifies a mosque. It appears that the model would be more confident if there were a spire emanating from the mosque dome. This suggests that mosques in the dataset may be biased towards having spikes. Finally the last column shows a white shark, interestingly the model will correct its error if the fin of the white shark becomes more bar like. This is actually a pattern with white sharks that models believe they should be seen near dive cages. Figure (refit) demonstrates this more clearly.

Correct Prediction Counterfactuals. For correct predictions label and prediction targeted attacks are equivalent. Figure 7 shows prediction targeted attacks which aim to answer:

Why did the model make this prediction?

For the first three columns the model seems to have learned a discriminative feature of the class. The african hunting dog's pattern was emphasized, the fireboat's water gun was moved to be more central to the image, and the axolotl's distinctive gills were highlighted. This suggests the model has learned these human interpretable features. We see again that the great white class has shown a cage like feature near the fin.



Figure 8: Label targeted counterfactual explanations ℓ_1 top-q attack with 20 iterations varying q and $\epsilon_0 = \epsilon * \sqrt{d}$.

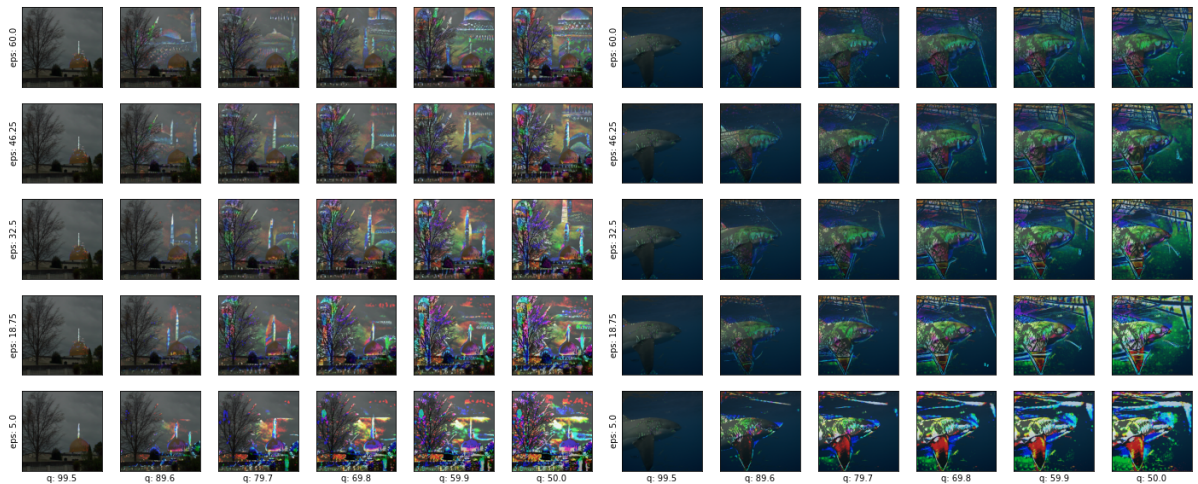


Figure 9: Label targeted counterfactual explanations ℓ_1 top-q attack with 20 iterations varying q and $\epsilon_0 = \epsilon * \sqrt{d}$. The perturbation has been magnified to emphasize sparsity.

6.1 Sweeps of Top-q parameters

Here we provide some additional images showing the effects of increasing the top q percentage and ϵ used in ℓ_1 top- q counterfactuals. Figures 8 and 10 show the variation in counterfactuals generated as q linearly decreases from 99.5 to 50.0 and $\epsilon_0 = \epsilon\sqrt{d}$ for ϵ increasing linearly from 5.0 to 60.0. Note that both images of white sharks seem to show the dive cage effect mentioned above. Figures 9 and 11 show the same counterfactuals but with the perturbations magnified and overlaid the original image to emphasize the sparsity changes. We clearly see an increase in sparsity as q decreases.

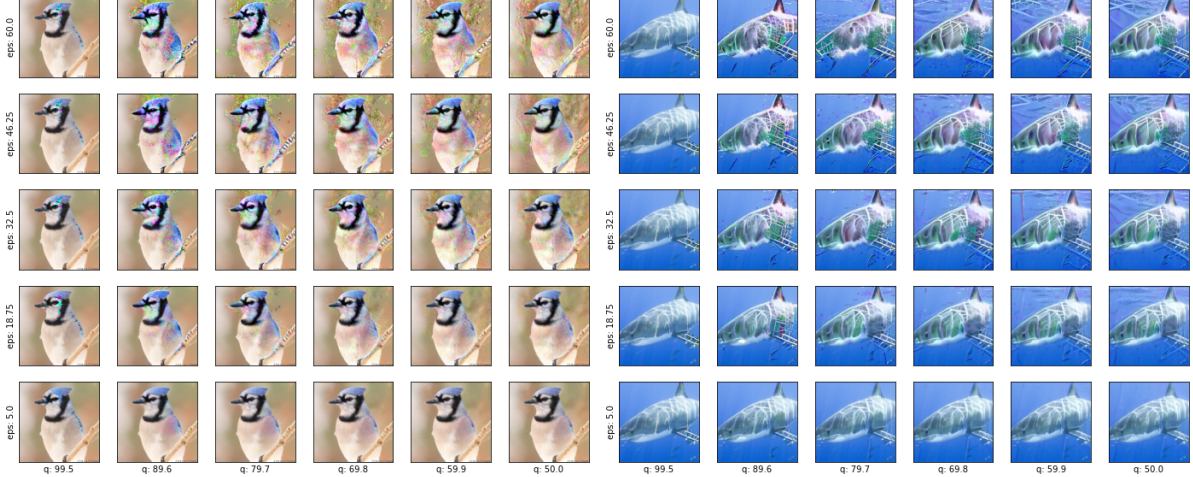


Figure 10: Label targeted counterfactual explanations ℓ_1 top-q attack with 20 iterations varying q and $\epsilon_0 = \epsilon * \sqrt{d}$.

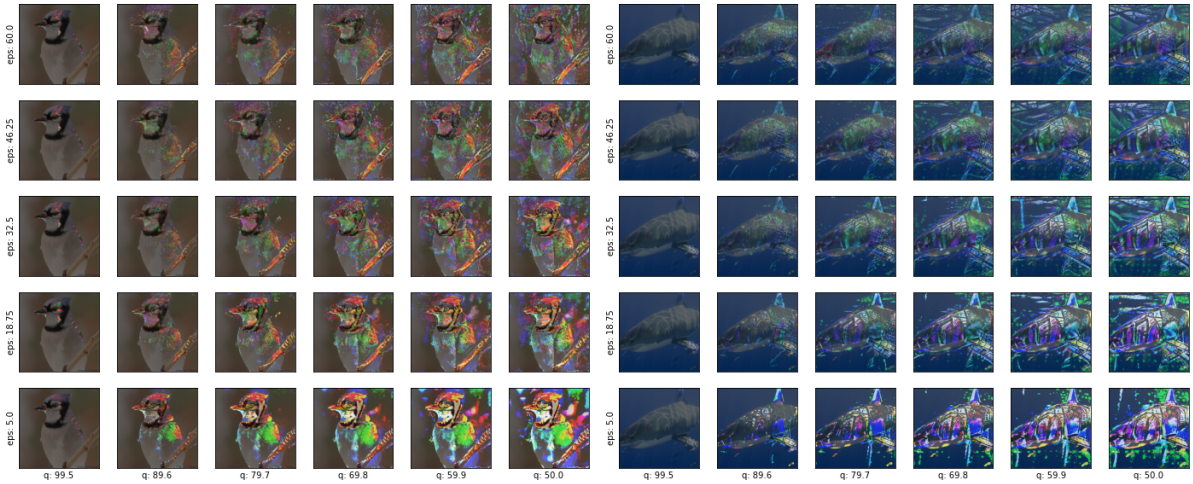


Figure 11: Label targeted counterfactual explanations ℓ_1 top-q attack with 20 iterations varying q and $\epsilon_0 = \epsilon * \sqrt{d}$. The perturbation has been magnified to emphasize sparsity.

References

Y. LeCun, Y. Bengio, and G. Hinton. Deep Learning. *Nature*, 521(7533):436–444, 2015.

Sundar Pichai. AI at Google: our principles, 2018. URL <https://www.blog.google/technology/ai/ai-principles/>.

Microsoft. Microsoft AI principles, 2019. URL <https://www.microsoft.com/en-us/ai/responsible-ai>.

C. Todd Lopez. DOD Adopts 5 Principles of Artificial Intelligence Ethics, 2020. URL <https://www.defense.gov/Explore/News/Article/Article/2094085/dod-adopts-5-principles-of-artificial-intelligence-ethics/>.

Ian J. Goodfellow, Jonathon Shlens, and Christian Szegedy. Explaining and harnessing adversarial examples. In International Conference on Learning Representations, 2015.

Alexey Kurakin, Ian J. Goodfellow, and Samy Bengio. Adversarial machine learning at scale. In International Conference on Learning Representations, 2017.

Andrew Slavin Ros and Finale Doshi-Velez. Improving the adversarial robustness and interpretability of deep neural networks by regularizing their input gradients. In AAAI Conference on Artificial Intelligence, 2018.

Aleksander Madry, Aleksandar Makelov, Ludwig Schmidt, Dimitris Tsipras, and Adrian Vladu. Towards deep learning models resistant to adversarial attacks. In *International Conference on Learning Representations*, 2018. URL <https://openreview.net/forum?id=rJzIBfZAb>.

Seyed-Mohsen Moosavi-Dezfooli, Jonathan Uesato, Alhussein Fawzi, and Pascal Frossard. Robustness via curvature regularization, and vice versa. In *IEEE Conference on Computer Vision and Pattern Recognition*, 2019. URL https://openaccess.thecvf.com/content_CVPR_2019/papers/Moosavi-Dezfooli_Robustness_via_Curvature-Regularization_and_Vice-Versa_CVPR_2019_paper.pdf.

Uri Shaham, Yutaro Yamada, and Sahand Negahban. Understanding adversarial training: Increasing local stability of supervised models through robust optimization. *Neurocomputing*, 2018.

Tsui-Wei Weng, Huan Zhang, Hongge Chen, Zhao Song, Cho-Jui Hsieh, Duane Boning, Inderjit S. Dhillon, and Luca Daniel. Towards fast computation of certified robustness for relu networks. In *ICML*, 2018.

Jonathan Uesato, Brendan O'Donoghue, Aaron van den Oord, and Pushmeet Kohli. Adversarial risk and the dangers of evaluating against weak attacks. In *ICML*, 2018.

Anish Athalye, Nicholas Carlini, and David Wagner. Obfuscated gradients give a false sense of security: Circumventing defenses to adversarial examples. In *ICML*, 2018.

Chuan Guo, Jacob R. Gardner, Yurong You, Andrew Gordon Wilson, and Kilian Q. Weinberger. Simple black box adversarial attacks. In *ICML*, 2019.

Jinghui Chen, Dongruo Zhou, Jinfeng Yi, and Quanquan Gu. A frank-wolfe framework for efficient and effective adversarial attacks. In *Thirty-Fourth AAAI Conference on Artificial Intelligence*, 2020.

Sebastian Bach, Alexander Binder, Gregoire Montavon, Frederick Klauschen, Klaus-Robert Muller, and Wojciech Samek. On pixel-wise explanations for non-linear classifier decisions by layer-wise relevance propagation. *PloS one*, 10(7), 2015.

Marco Ribeiro, Sameer Singh, and Carlos Guestrin. why should i trust you? explaining the predictions of any classifier. In *ACM SIGKDD Intl. Conference on Knowledge Discovery and Data Mining*, 2016.

Amit Dhurandhar, Pin-Yu Chen, Ronny Luss, Chun-Chen Tu, Paishun Ting, Karthikeyan Shanmugam, and Payel Das. Explanations based on the missing: Towards contrastive explanations with pertinent negatives. In *NeurIPS*, 2019.

Andrew Ilyas, Shibani Santurkar, Dimitris Tsipras, Logan Engstrom, Brandon Tran, and Aleksander Madry. Adversarial examples are not bugs, they are features. In *NeurIPS 2019*, 2019.

Christian Etmann, Sebastian Lunz, Peter Maass, and Carola-Bibiane Schonlieb. On the connection between adversarial robustness and saliency map interpretability. In *ICML*, 2019.

Sandra Wachter, Brent Mittelstadt, and Chris Russell. Counterfactual explanations without opening the black box: Automated decisions and the gdpr. *Harvard Journal of Law & Technolog*, 31(2), 2018.

Dimitris Tsipras, Shibani Santurkar, Logan Engstrom, Alexander Turner, and Aleksander Madry. Robustness may be at odds with accuracy. In *International Conference on Learning Representations*, 2019. URL <https://openreview.net/forum?id=SyxAb30cY7>.

Nicolas Papernot, Patrick McDaniel, Ian Goodfellow, Somesh Jha, Z. Berkay Celik, and Ananthram Swami. Practical black-box attacks against machine learning. In *arXiv:1602.02697v4*, 2017.

H. Zhang, Y. Yu, J. Jiao, E. P. Xing, L. El Ghaoui, and M. I. Jordan. Theoretically principled trade-off between robustness and accuracy. In *ICML*, 2019.

Chunchuan Lyu, Kaizhu Huang, and Ha-Ning Liang. A unified gradient regularization family for adversarial examples. In *IEEE International Conference on Data Mining (ICDM)*, 2015.

Chongli Qin, James Martens, Sven Gowal, Dilip Krishnan, Krishnamurthy Dvijotham, Alhussein Fawzi, Soham De, Robert Stanforth, and Pushmeet Kohli. Adversarial robustness through local linearization. In *NeurIPS*, 2019.

Ramaravind K. Mothilal, Amit Sharma, and Chenhao Tan. Explaining machine learning classifiers through diverse counterfactual explanations. In *Conference on Fairness, Accountability, and Transparency*, 2020.

Amir-Hossein Karimi, Gilles Barthe, Borja Balle, and Isabel Valera. Model-agnostic counterfactual explanations for consequential decisions. In *AISTATS*, 2020.

Pouya Samangouei, Ardavan Saeedi, Liam Nakagawa, and Nathan Silberman. Explaingan: Model explanation via decision boundary crossing transformations. In *ECCV*, 2018.

Chun-Hao Chang, Elliot Creager, Anna Goldenberg, and David Duvenaud. Explaining image classifiers by counterfactual generation. In *ICLR*, 2019.

K. Xu, S. Liu, P. Zhao, P.-Y. Chen, H. Zhang, Q. Fan, D. Erdogmus, Y. Wang, and X. Lin. Structures adversarial attack: Towards general implementation and better interpretability. In ICLR, 2019.

E. Wong, L. Rice, and J. Z. Kolter. Fast is better than free: Revisiting adversarial training. In ICLR, 2020.

Yisen Wang, Xingjun Ma, JAMES Bailey, Jinfeng Yi, Bowen Zhou, and Quanquan Gu. On the convergence and robustness of adversarial training. In ICML, 2019.

M. Frank and P. Wolfe. An algorithm for quadratic programming. Naval research logistics quarterly, 3:95–110, 1956.

Martin Jaggi. Revisiting frank-wolfe: Projection-free sparse convex optimization. In ICML, pages 427–435, 2013.

Simon Lacoste-Julien. Convergence rate of frank-wolfe for non-convex objectives. In arXiv: 1607.00345, 2016.

Jarrid Rector-Brooks, Jun-Kun Wang, and Barzan Mozafari. Revisiting projection-free optimization for strongly convex constraint sets. In AAAI, 2019.

Shibani Santurkar, Dimitris Tsipras, Andrew Ilyas, and Aleksander Madry. How does batch normalization help optimization? In NeurIPS, 2018.

Zeyuan Allen-Zhu, Yuanzhi Li, and Zhao Song. A convergence theory for deep learning via over-parameterization. In ICML, 2019.

Difan Zou and Quanquan Gu. An improved analysis of training over-parameterized deep neural networks. In NeurIPS, 2019.

Yuan Cao and Quanquan Gu. Generalization error bounds of gradient descent for learning over-parameterized deep relu networks. In AAAI, 2020.

Dimitri P. Bertsekas. Nonlinear Programming. Athena Scientific, 1999.

Q. Vera Liao, Daniel Gruen, and Sarah Miller. Questioning the ai: Informing design practices for explainable ai user experiences. In Conference on Human Factors in Computing Systems, 2020.

Shubham Sharma, Jette Henderson, and Joydeep Ghosh. Certifai: A common framework to provide explanations and analyse the fairness and robustness of black-box models. In AIS, 2020.

Shibani Santurkar, Andrew Ilyas, Dimitris Tsipras, Logan Engstrom, Brandon Tran, and Aleksander Madry. Image synthesis with a single (robust) classifier. In NeurIPS, 2019.

Logan Engstrom, Andrew Ilyas, Shibani Santurkar, and Dimitris Tsipras. Robustness (python library), 2019. URL <https://github.com/MadryLab/robustness>.

Maksym Andriushchenko, Francesco Croce, Nicolas Flammarion, and Matthias Hein. Square attack: a query-efficient black-box adversarial attack via random search. In ECCV, 2020.

Jia Deng, Wei Dong, Richard Socher, Li-Jia Li, Kai Li, and Li Fei-Fei. Imagenet: A large-scale hierarchical image database. In 2009 IEEE conference on computer vision and pattern recognition, pages 248–255. Ieee, 2009.

Daniel Kang, Yi Sun, Tom Brown, Dan Hendrycks, and Jacob Steinhardt. Transfer of adversarial robustness between perturbation types. arXiv preprint arXiv:1905.01034, 2019.